


Large Eddy Simulation of a Turbulent Diffusion Flame: Some Aspects of Subgrid Modelling Consistency

J. Ventosa-Molina¹  · O. Lehmkuhl^{1,2} ·
C. D. Pérez-Segarra¹ · A. Oliva¹

Received: 5 April 2016 / Accepted: 3 April 2017 / Published online: 26 April 2017
© Springer Science+Business Media Dordrecht 2017

Abstract In the context of Large Eddy Simulation (LES) solely for the momentum transport equation there may be found several models for the turbulent subgrid fluxes. Furthermore, among those relying on the eddy diffusivity approach, each model may be based on different invariants of the strain rate. Besides, when heat and mass transfer are also considered, closures for the subgrid turbulent scalar fluxes are also required. Hence, different model combinations may be considered. Additionally, when other physical phenomena are included, such as combustion, further subgrid modelling is involved. Therefore, in the present study a LES simulation of a turbulent diffusion flame is performed and different combination of subgrid models are used in order to analyse the numerical effects in the simulations. Several models for the turbulent momentum subgrid fluxes are considered, both constant and dynamically evaluated Schmidt numbers. Regarding combustion, in the context of the Flamelet/Progress-Variable (FPV) model, with an assumed probability density function for the turbulent-chemistry interactions and four different closures for the subgrid mixture fraction variance are considered. Hence, a large number of model combinations are possible. The present study highlights the need for a consistent closure of subgrid effects. It is shown that, in the context of an FPV modelling, incorrect capture of subgrid mixing results in a flame lift-off for the studied flame (DLR A diffusion flame), even though experimentally an attached flame was reported. It is found that a consistent formulation is required, that is, all subgrid closures should become active in the same regions of the domain to avoid modelling inconsistencies. In contrast, when the classical flamelet approach is used, no

✉ J. Ventosa-Molina
jordivm@cttc.upc.edu

✉ A. Oliva
cttc@cttc.upc.edu

¹ Heat and Mass Transfer Technological Center (CTTC), Universitat Politècnica de Catalunya-BarcelonaTech (UPC) ESEIAAT, Colom 11, E-08222 Terrassa, Barcelona, Spain

² Barcelona Supercomputing Center (BSC), Barcelona, Spain

lift-off is observed. The reason is that the classical flamelet includes only a limited subset of the possible flame states, i.e. only includes burning flamelets and extinguished flamelets for scalar dissipation rates past the extinction one.

Keywords Turbulent diffusion flame · Mixture fraction variance · Subgrid scalar dissipation rate · Flamelet/progress-variable · Turbulence modelling

1 Introduction

Research in the past decades has put at the disposal of researchers and designers advanced modelling tools for the simulation of fluid dynamics. Nowadays, Direct Numerical Simulations (DNS) of the Navier-Stokes (NS) equations are becoming more affordable. However, computational requirements for those simulations are still too high for most cases of academic and industrial interest. Models such as Reynolds Averaged Navier Stokes Simulations (RANS) and Large Eddy Simulations (LES) require much lower computational resources at the expense of a higher modelling effort. In the former, the NS equations are temporally averaged, requiring the modelling of all flow scales. On the other hand, in LES only the small scales, which have a more universal behaviour, are modelled, whereas the large motions of the flow, which are more case dependent, are resolved.

In this regard, in LES all flow phenomena occurring at scales smaller than the grid or filter resolution have to be modelled. Beginning with the momentum equations, closure is required for the turbulent subgrid fluxes. In the past decade much effort has been devoted to accurately model them and this is still an ongoing topic of research [1–4]. Analogously, when energy transport is considered, subgrid fluxes also require closure. Nevertheless, in this aspect, common approaches are to assume a constant turbulent Prandtl number or to dynamically evaluate the turbulent Prandtl number [5]. Analogously, when species transport is considered these two strategies are also commonly employed for the Schmidt number.

When additional physics are considered, such as combustion, multiphase flow, particles transport, etc., further subgrid models are required. Concerning combustion phenomena, chemistry occurs at the molecular level. Thus, in most cases, chemistry mostly takes place at the subgrid level and consequently requires modelling. If chemistry is assumed to take place in thin laminar layers embedded within turbulent flow structures [6], flow eddies can be assumed not to penetrate the reaction layer of the flame. In this context, and focusing on diffusion flames, the combustion process may be split into a transport process and a diffusion-reaction process. The former may be resolved in a preprocessing stage and stored in a chemical database as a function of a reduced set of parameters, provided that turbulence-chemistry interactions are assumed. This is usually achieved through assumed probability density functions (*pdf*). In the Flamelet/Progress-variable model [7] the mixture fraction Z , a mixing tracker, and a progress-variable c , a reaction progress tracker, are used. Then a β – *pdf* is a common choice to characterise turbulence-chemistry interactions. This *pdf* applied to the mixing process is defined through the first moment and second central moment of the mixture fraction, namely \bar{Z} and Z_v .

In LES, mixing at the subfilter level can be characterised through two interconnected quantities, the subgrid mixture fraction variance Z_v and the subgrid scalar dissipation rate χ_{sgs} . The modelling of both quantities has received significant attention over the last years and consequently, several models can be found in the literature: ranging from an equilibrium model [8], to transport equations for the variance itself [9] or through the second moment of the mixture fraction, $\overline{Z^2}$ [10, 11]. These last two approaches require additional

modelling for the subgrid scalar dissipation rate. Closure may be achieved through algebraic expressions using a turbulent time-scale [9, 10]. Alternatively, closure for the scalar dissipation rate can also be performed solving a transport equation for the filtered squared gradient of the mixture fraction [11]. Regarding the equilibrium model, although being computationally efficient, it has been reported to produce erroneous estimations of the scalar mixing in technically relevant flow configurations [10].

As it can readily be seen several modelling options are available, relying on different approaches. Furthermore, each one involves different equations using different closures. Additionally, the subgrid variance and subgrid scalar dissipation rate are parameters of the flamelet database. Thus, differences in their predictions will result in different retrieved values from the flamelet database, and will lead to different flame dynamics.

In the present work the DLR simple-jet [12, 13] is selected as study case. It features a fuel jet, which is a mixture of CH_4 , H_2 and N_2 , surrounded by a coflowing stream of oxidiser. Experimentally this flame is attached to the fuel nozzle rim. The stabilisation mechanism for this flame is then mostly due to diffusion through the shear layer between the two reactant streams. Hence, proper characterisation of subgrid mixing is critical for this case.

Due to its canonical geometry and configuration, this flame has been extensively used to validate several combustion models. Kempf et al. [14] analysed the modelling capacities of a flamelet model in the context of LES using this flame. Pitsch [15] applied the classical unsteady flamelet model to study differential diffusion effects in this flame. Emami and Eshghinejad Fard [16] used this flame to study a flamelet approach with Artificial Neural Networks. Lindsted and Ozarovsky [17] used a *pdf* model, Vogiatzaki [18] applied a Multiple Mapping Conditioning (MMC) model and Wang and Pope [19] tested a LES/*pdf* model coupled with a Flamelet/Progress-variable (FPV) model. Fairweather and Woolley [20] used a first order CMC model to study several chemical mechanisms. Lee and Choi [21, 22] used an Eulerian Particle Flamelet model (EPFM) to study NO emissions. Ihme et al. [23, 24] performed a LES simulation using a Flamelet/Progress-Variable model to study combustion generated noise. Kemenov et al. [25, 26] performed LES simulations of this case using a single flamelet in order to study molecular diffusion effects in the former and two different subgrid mixture fraction closures in the latter. Most of these studies were conducted using RANS approaches, where turbulent diffusivity models usually give extra non-physical diffusion, or with *pdf* methods, where mixing itself requires closure [27]. Unlike RANS, in LES only the subgrid scales are involved in the evaluation of the turbulent diffusivity, while the large scales are directly accounted for. Furthermore, in combustion phenomena molecular transport is enhanced due to the exothermicity of chemical reactions [25]. Both Wang and Pope [19] and Ihme et al. [24] reported LES simulations using a FPV model, where a single flamelet was used in the former and only the steady burning solutions were included in the latter [23].

In this context, the paper aims to study the interaction between different subgrid models in the context of a diffusion flame. Different models for subgrid variance and subgrid scalar dissipation rate together with several models for the Reynolds stress tensor and subgrid turbulent scalar fluxes are used. Furthermore, their effect in predicted profiles and flame stabilisation are compared. Thus, the study focuses on different implementations of subgrid modelling, which are based on different physical principles, and their effect on the flame predictions. Additionally, the thermal effects of the flame on the shear layer are also discussed.

The paper is organized as follows: first, the mathematical formulation for the LES model, the combustion model and subgrid closures are presented. The experimental case and computational domain are then described. Afterwards, results are shown, focusing first

on the turbulent momentum and scalar subgrid fluxes modelling, then in the subgrid mixing closure.

2 Mathematical Model

In the following the modelling of flow and chemistry is detailed. First, the LES framework is described and closures for the turbulent subgrid fluxes are discussed. Next, the Flamelet/Progress-Variable model is described in the context of LES. Finally, closure for the subgrid terms of the flamelet database are presented, namely for the subgrid mixture fraction variance and subgrid scalar dissipation rate.

2.1 Large Eddy simulation

LES describes the motion of the large scales of the flow, whereas the small scales are modelled. Scale splitting is performed by means of a low-pass filter,

$$\overline{\rho\phi} = \int_{\Omega} \rho\phi G(\mathbf{x}, \xi) d\xi \quad (1)$$

In grid based filtering, the filter kernel $G(\mathbf{x}, \xi)$ becomes a top-hat filter with size $\Delta = (V)^{1/3}$, where V is the mesh cell volume. Additionally, for variable density flows, the filtered quantities are density weighted, or Favre filtered. Favre filtered quantities can be related to Reynolds filtered quantities through $\overline{\rho\phi} = \overline{\rho}\tilde{\phi}$. Therefore, after performing the filtering operation, the filtered low-Mach Navier-Stokes equations are:

$$\frac{\partial \overline{\rho}}{\partial t} + \frac{\partial \overline{\rho\tilde{u}_j}}{\partial x_j} = 0 \quad (2)$$

$$\frac{\partial \overline{\rho\tilde{u}_i}}{\partial t} + \frac{\partial \overline{\rho\tilde{u}_j\tilde{u}_i}}{\partial x_j} = -\frac{\partial \overline{p}}{\partial x_i} + \frac{\partial}{\partial x_j} \left((\tilde{\mu} + \mu_t)\tilde{\sigma}_{ij} \right) + \overline{\rho}g_i \quad (3)$$

where $\overline{\rho}$, \overline{p} and \tilde{u}_i represent the filtered density, the filtered dynamic pressure and the Favre filtered velocity, respectively. This system of equations is completed with the energy and species equations, which are discussed in the following in the context of the combustion model. The diffusive fluxes are $\tilde{\sigma}_{ij} = \left(\frac{\partial \tilde{u}_i}{\partial x_j} + \frac{\partial \tilde{u}_j}{\partial x_i} - \frac{2}{3}\delta_{ij}\frac{\partial \tilde{u}_k}{\partial x_k} \right)$. Turbulent subgrid fluxes have been modelled through an eddy-diffusivity assumption, where the choice of subgrid turbulence model is discussed along with the model for the subgrid scalar turbulent diffusivity in Section 4.1. Closures for the Reynolds stress tensor have been extensively studied [1, 3, 4] and new models are still nowadays being postulated [28, 29]. Regarding the unresolved fluxes for the scalars, such as the temperature or the mixture fraction, usually a turbulent Prandtl, Schmidt or Lewis number is used. These non-dimensional numbers are either constant or dynamically evaluated in a similar manner as in the Dynamic Eddy Viscosity model (DEV) [1, 5]. Thus, there is a wide range of closure combinations.

Thermochemical properties, such as the density and molecular diffusivities, are provided by the combustion model, and are discussed in the following.

2.2 Flamelet/progress-variable (FPV) model

In the flamelet regime, chemically active layers are thinner than the size of the Kolmogorov scale. Therefore, it is justified to assume that turbulent eddies do not penetrate the reaction zone. Thus, the flame can be considered to exist in a quasi-laminar flow field within those

eddies [6]. Consequently, the flame can be considered as an ensemble of laminar flames surrounded by turbulent structures, capable only of wrinkling and straining the flame.

Hence, defining a new coordinate system described by the mixture fraction, Z , and applying a coordinate transformation to the species and energy equations the flamelet equations are obtained. The full equations are not reproduced here for the sake of brevity, the reader is referred to the Eqs. 24 and 25 of the paper by Pitsch and Peters [30]. In compact form they are

$$\rho \frac{\partial \phi}{\partial t} = \rho \frac{\chi_Z}{2} \frac{\partial^2 \phi}{\partial Z^2} + S_\phi \tag{4}$$

where ϕ denotes either species mass fractions or temperature, S_ϕ includes the equation’s source term and additional transport terms. $\chi_Z = 2D_z \left(\frac{\partial Z}{\partial x_i} \frac{\partial Z}{\partial x_i} \right)$ is the scalar dissipation rate, where D_Z is the mixture fraction diffusivity. χ_Z introduces flow effects from the transport process into the diffusion-chemistry process. Through an analogy between diffusion flames in the flamelet regime and counterflow flames [6], the scalar dissipation rate can be described through an analytical expression in mixture fraction space

$$\chi_Z(Z) = \chi_{st} \frac{f(Z)}{f(Z_{st})} \tag{5a}$$

$$f(Z) = \exp(-2[erfc^{-1}(2Z)]^2) \tag{5b}$$

where $erfc^{-1}$ is the inverse of the complementary error function and χ_{st} is the scalar dissipation rate at the stoichiometric mixture fraction. Furthermore, this expression was also derived from the analysis of unsteady mixing layers [6].

Flamelet modelling of diffusion flames offers a dimensionality reduction by mapping the multicomponent diffusion-reaction process into a limited set of transported scalars. In the classical flamelet, solutions of one-dimensional flamelets in their steady state form can be expressed as a state relation

$$\phi = \xi_\phi(Z, \chi_{st}) \tag{6}$$

Plotting the stoichiometric temperature as a function of the stoichiometric scalar dissipation rate the S-shaped curve is obtained, Fig. 1.

The upper branch of this curve represents the stable burning state, the middle one the unstable burning solution and the lower one the extinguished state or pure mixing. The

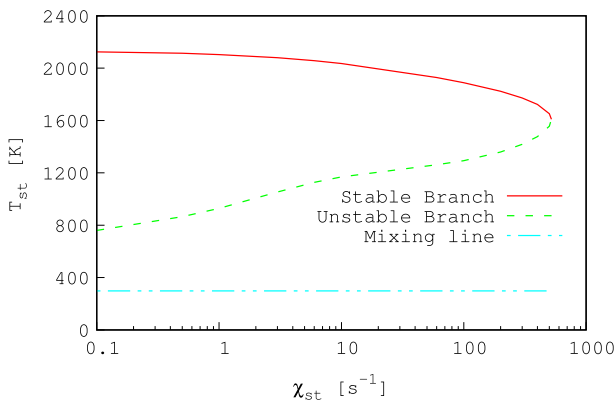


Fig. 1 S-shaped curve for the DLR Flame. Dotted region represents the radiation accessible flamelet subspace

turning point between the upper and lower branch corresponds to the quenching scalar dissipation χ_q . Although with (4) all solutions of the S-shaped curve can be obtained by setting Z and χ_{st} , (6) does not offer a unique representation of the curve. Hence, only one branch can be represented. Applications of the flamelet model typically represent only the stable burning branch and the stable non-burning solution for $\chi_{st} > \chi_q$. This shortcoming of flamelet models can be overcome by replacing χ_{st} by a new flamelet parameter $\Lambda = c|Z_{st}$, as proposed by Pierce and Moin [7], where the progress-variable c is usually defined as the summation of several species mass fractions. The Λ parameter is required in order to ensure statistical independence between database parameters. However, it is more convenient to solve a transport equation for the progress-variable itself. Consequently, the database is stated as a function of Z and c , which in turn implies a bijective relation between Λ and c . In other words, the progress-variable must be able to identify each flamelet solution unambiguously.

Besides the previous discussion, computation of the variable density LES equations yields Favre filtered quantities. Therefore, in order to access the flamelet database, these parameters have to be restated in terms of turbulent Favre filtered quantities. Chemistry-turbulence interactions are modelled through assumed probability density functions (*pdf*). The assumed *pdfs* are a $\beta - pdf$ for the mixture fraction and a $\delta - pdf$ for the progress-variable. The former is described through the mean \tilde{Z} and the variance Z_v . The latter uses only the mean \tilde{c} . The resulting state relation for turbulent cases is

$$\tilde{\phi} = \tilde{F}_\phi(\tilde{Z}, Z_v, \tilde{c}) \tag{7}$$

In the present work the FPV model is used in two different ways. On the one hand, one database is created including all solutions lying on the S-shaped curve: ignited, partially ignited and the mixing line. This approach is referred to as the steady FPV (SFPV) database. On the other hand, it is used to emulate the classical flamelet (FM) by creating a flamelet database which only includes solution of the ignited branch, but using the database in the form of (7) instead of the turbulent counterpart of (6). A drawback of the classical flamelet is that it cannot represent partially ignited/extinguished stated. It is here included as a reference case to evidence the effect of a limited thermochemical database.

A last aspect to define is the form of the progress-variable. It is a tracking quantity which, together with the mixture fraction, must uniquely define the thermochemical state. It is usually defined as a linear summation, or in some cases a weighted summation, of several species. In the present case, a linear combination of CO , CO_2 , H_2 and H_2O is used. The GRI 3.0 mechanism [31] has been used to generate the chemical database and differential diffusion effects have been included in the solution of the flamelet equations.

The flamelet database is discretised using 100x25x100 points for the mixture fraction, its variance and the progress-variable, respectively.

In order to retrieve the data from the database, the Favre filtered mixture fraction \tilde{Z} , its subfilter variance Z_v and progress variable \tilde{c} are computed in physical space. Both mixture fraction and progress-variable are transported quantities in physical space

$$\bar{\rho} \frac{\partial \tilde{Z}}{\partial t} + \bar{\rho} \tilde{u}_j \frac{\partial \tilde{Z}}{\partial x_j} = \frac{\partial}{\partial x_j} \left(\bar{\rho} (\tilde{D}_Z + D_{Z,t}) \frac{\partial \tilde{Z}}{\partial x_j} \right) \tag{8}$$

$$\bar{\rho} \frac{\partial \tilde{c}}{\partial t} + \bar{\rho} \tilde{u}_j \frac{\partial \tilde{c}}{\partial x_j} = \frac{\partial}{\partial x_j} \left(\bar{\rho} (\tilde{D}_c + D_{c,t}) \frac{\partial \tilde{c}}{\partial x_j} \right) + \tilde{w}_c \tag{9}$$

where \tilde{D}_Z and \tilde{D}_c are the mixture fraction and progress-variable molecular diffusivities, respectively. Analogously, $D_{Z,t}$ and $D_{c,t}$ are the turbulent diffusivities. As previously

stated, two closures are considered, a dynamic evaluation of the turbulent Schmidt or using a constant Schmidt number $Sc_t = 0.4$. The progress-variable reaction rate \tilde{w}_c is defined as the summation of the reaction rates of the species defining the progress-variable. The mixture fraction variance is not readily available and requires modelling. Several closures are discussed in the following section.

2.2.1 Combustion subgrid closures

The variance Z_v , or second central moment, which is required to retrieve solutions from the FPV database, is defined in terms of a probability density function [32]

$$Z_v = \tilde{Z}^2 - \tilde{Z}^2 \tag{10}$$

It can be computed by either using a transport equation for the variance itself [32] (VTE)

$$\bar{\rho} \frac{\partial Z_v}{\partial t} + \bar{\rho} \tilde{u} \frac{\partial Z_v}{\partial x_i} = \frac{\partial}{\partial x_i} \left(\bar{\rho} (\tilde{D}_Z + D_{Z,t}) \frac{\partial Z_v}{\partial x_i} \right) + 2\bar{\rho} (\tilde{D}_Z + D_{Z,t}) \frac{\partial \tilde{Z}}{\partial x_i} \frac{\partial \tilde{Z}}{\partial x_i} - \bar{\rho} \tilde{\chi}_Z \tag{11}$$

or through a transport equation for the second moment of the mixture fraction \tilde{Z}^2 (STE) [11]

$$\bar{\rho} \frac{\partial \tilde{Z}^2}{\partial t} + \bar{\rho} \tilde{u} \frac{\partial \tilde{Z}^2}{\partial x_i} = \frac{\partial}{\partial x_i} \left(\bar{\rho} (\tilde{D}_Z + D_{Z,t}) \frac{\partial \tilde{Z}^2}{\partial x_i} \right) - \bar{\rho} \tilde{\chi}_Z \tag{12}$$

A further parameter is here introduced to characterise the mixing state, the filtered scalar dissipation rate $\tilde{\chi}_Z$. In both cases closure for the scalar dissipation rate is required

$$\tilde{\chi}_Z = 2\tilde{D}_Z \frac{\partial \tilde{Z}}{\partial x_i} \frac{\partial \tilde{Z}}{\partial x_i} = 2\tilde{D}_Z \frac{\partial \tilde{Z}}{\partial x_i} \frac{\partial \tilde{Z}}{\partial x_i} + \chi_{Z,sgs} \tag{13}$$

where $\chi_{Z,sgs} = 2\tilde{D}_Z \left(\frac{\partial \tilde{Z}}{\partial x_i} \frac{\partial \tilde{Z}}{\partial x_i} - \frac{\partial \tilde{Z}}{\partial x_i} \frac{\partial \tilde{Z}}{\partial x_i} \right)$ is the subfilter dissipation rate.

Even though the VTE and STE models are equivalent at the continuous level through (10), Kemenov et al. [26] and Kaul et al. [33] showed that they are not exactly equivalent at the discrete level. For example, the effect of the squared gradient is opposite between the two models. In the STE model $2\tilde{D}_Z \frac{\partial \tilde{Z}}{\partial x_i} \frac{\partial \tilde{Z}}{\partial x_i}$ is a dissipation term and in the VTE model $2D_{Z,t} \frac{\partial \tilde{Z}}{\partial x_i} \frac{\partial \tilde{Z}}{\partial x_i}$ is a production term. Therefore, discretisation errors in the computation of the gradient or differences in the mixture fraction field will have a different impact in each model.

Both STE and VTE require closure for χ_{sgs} . In (11), if production and destruction of the mixture fraction variance at the small scales are assumed to be in equilibrium [8, 34], denoted as the Local Equilibrium Assumption (LEA), the scalar dissipation rate becomes

$$\tilde{\chi}_Z = 2(\tilde{D}_Z + D_{Z,t}) \frac{\partial \tilde{Z}}{\partial x_i} \frac{\partial \tilde{Z}}{\partial x_i} \tag{14}$$

However, with the LEA the mixture fraction variance requires a model, as (11) with this assumption is just the transport equation of a passive scalar. Hence, a scale similarity model [8] for the mixture fraction variance may be used

$$\bar{\rho} Z_v = C_{var} \Delta^2 \bar{\rho} |\nabla \tilde{Z}| \tag{15}$$

where C_{var} is here calculated using the *Leonard term Expansion Dynamic model* (LED) [35].

If non-equilibrium effects are to be considered, (14) cannot be used. Thus, alternative closures for the subfilter dissipation rate have to be used. Models using either an algebraic

closure or a transport equation for the filtered gradient of the mixture fraction have been proposed.

On the one hand, the subgrid variance can be related to the subfilter dissipation rate through a turbulent mixing time-scale [9, 10], the algebraic approach,

$$\chi_{Z,sgs} = \frac{C_Z}{\tau} Z_v = C_Z \frac{\nu_t}{\Delta^2} Z_v \tag{16}$$

$$\frac{1}{\tau} = \frac{\varepsilon_{sgs}}{k_{sgs}} \approx \frac{2C_S \Delta^2 |\widetilde{S}| \widetilde{S}_{ij} \widetilde{S}_{ij}}{2C_k \Delta^2 \widetilde{S}_{ij} \widetilde{S}_{ij}} \approx \frac{\nu_t}{\Delta^2} \tag{17}$$

where τ is a turbulent (mixing) time-scale, k_{sgs} and ε_{sgs} are the subgrid turbulent kinetic energy and dissipation, respectively. The turbulent viscosity ν_t is used to model the latter. The model constant is of the form $C_Z = C_{\chi,Z}(C_\varepsilon/C_u)$, where $C_{\chi,Z} = 2$ is a constant relating mechanical and scalar time-scales and $(C_\varepsilon/C_u) = 2$ is related to the energy spectra [9]. Nevertheless, the effect of the constant is afterwards investigated. In the context of RANS models, a similar functional relation between χ_{sgs} and Z_v was proposed. The time-scale is related to the ratio of kinetic energy and kinetic energy dissipation and the constant takes a value of 2 [6].

On the other hand, closure for the scalar dissipation rate $\widetilde{\chi}_Z$ can be achieved by constructing a transport equation for the filtered squared gradient $|\widetilde{\nabla Z}|^2$ [11], here denoted as SDR-TE. Evaluation of the SDR-TE requires modelling several unclosed terms and the evaluation of computationally expensive terms.

$$\begin{aligned} \frac{D}{Dt} (\overline{\rho |\widetilde{\nabla Z}|^2}) &= \frac{\partial}{\partial x_i} \left(\overline{\rho} (\widetilde{D}_Z + D_{Z,t}) \frac{\partial |\widetilde{\nabla Z}|^2}{\partial x_i} \right) \\ &\quad - 2\overline{\rho} \left(\frac{\partial \widetilde{u}_i}{\partial x_j} \frac{\partial \widetilde{Z}}{\partial x_i} \frac{\partial \widetilde{Z}}{\partial x_j} \right) - 2\overline{\rho} \widetilde{D}_Z \left(\frac{\partial^2 \widetilde{Z}}{\partial x_i \partial x_j} \right)^2 \\ &\quad - \frac{2}{\overline{\rho}} \frac{\partial \overline{\rho}}{\partial x_i} \frac{\partial \widetilde{Z}}{\partial x_i} \left(\frac{\partial}{\partial x_j} \left(\overline{\rho} \widetilde{D}_Z \frac{\partial \widetilde{Z}}{\partial x_j} \right) \right) \\ &\quad + 2 \frac{\partial \overline{\rho} \widetilde{D}_Z}{\partial x_i} \frac{\partial \widetilde{Z}}{\partial x_i} \left(\frac{\partial^2 \widetilde{Z}}{\partial x_j^2} \right) + 2 \frac{\partial \widetilde{Z}}{\partial x_i} \frac{\partial \widetilde{Z}}{\partial x_j} \left(\frac{\partial^2 \overline{\rho} \widetilde{D}_Z}{\partial x_i \partial x_j} \right) \\ &\quad + C_{prd} \overline{\rho} \frac{32\nu_t}{\Delta^2} \left(|\widetilde{\nabla Z}|^2 - |\nabla \widetilde{Z}|^2 \right) \\ &\quad - 12C_{var} \overline{\rho} \frac{\widetilde{D}_Z}{Z_v} \left(|\widetilde{\nabla Z}|^2 - |\nabla \widetilde{Z}|^2 \right)^2 \end{aligned} \tag{18}$$

where $C_{prd} = 1$ is a model constant and C_{var} is dynamically evaluated using the LED model, as performed for the LEA model (15). For further details on the different terms of this equation the reader is referred to the paper by Knudsen et al. [11]

Summarizing, the four closures used in the following are listed in Table 1.

2.3 Numerical method

A finite-volume approach is used to solve the different transport equations, particularly 3D collocated meshes, either structured or unstructured. In order to preserve kinetic energy, a symmetry-preserving scheme [36] is used in the construction of the discrete convective term of the momentum equation. For the scalar convective terms, a SMART scheme is used [37]. A second order centred difference scheme is used to construct the discrete diffusive term for all transported quantities. For filtering operations, a top-hat test filter with filter size $\hat{\Delta} = 2\Delta$ is used. Temporal integration is performed using a linear multi-step method, with a second order Adams-Bashforth scheme in the predictor step and a Crank-Nicholson scheme in the corrector step. The pressure-velocity coupling is solved through a Fractional Step method. The Poisson equation is solved by means of FFT-based Poisson Solver by Borrell et al. [38], due to the use of an axisymmetric mesh with one circulating direction, as described in the next section.

Numerical computations are performed using the general purpose unstructured and parallel object-oriented Computational Fluid Dynamics (CFD) code TermoFluids [39].

3 Turbulent Diffusion $CH_4/H_2/N_2$ Flame - DLR A Flame

The case of study is the axisymmetric jet flame denoted as DLR Flame A [12, 13, 40], which was a standard flame used in the third “International Workshop on Measurement and Computation of Turbulent Nonpremixed Flames” (TNF Workshop) [41]. It consists of a $D = 8\text{mm}$ wide fuel jet with a thinned rim at the exit. The inner fuel jet is a mixture of 33.2% H_2 , 22.1% CH_4 , and 44.7% N_2 by volume and the outer jet is regular air with 20.1% O_2 . The fuel jet exit bulk velocity is fixed to $V_b = 42.15\text{m/s}$, resulting in a Reynolds number of $Re_b = 15,200$. The jet was mounted concentrically to the coflow nozzle, which had a diameter of 140mm and provided air at 0.3m/s . Both fuel and coflow air were at 300K . The stoichiometric mixture fraction is $Z_{st} = 0.167$.

Regarding the computational mesh, mainly two grids have been used, a fine and a coarse one, both 60D long in the axial direction. The former is a structured collocated mesh concentrated near the central jet with $95 \times 645 \times 32$ control volumes (CV) in the radial, axial and azimuthal directions respectively. Mesh sizes were compared against an estimated Kolmogorov scale for this case, and ratios ranging between 15 and 20 were found in the regions of interest. According to Pope [27] motions for the bulk dissipation are within lengthscales 8 and 60 times the Kolmogorov scale, with the peak falling at around 24. Thus, the current

Table 1 List of subgrid mixing closures and the equations involved in each model

| | Z_v | χ_{sgs} |
|--------|--------------------|--------------|
| LEA | Eq. (15) | Eq. (14) |
| VTE | Eq. (11) | Eq. (16) |
| STE | Eq. (10), Eq. (12) | Eq. (16) |
| SDR-TE | Eq. (10), Eq. (12) | Eq. (18) |

mesh is capable of capturing most of the bulk dissipation. The coarse mesh was an unstructured mesh which featured around 250 kCV, using 16 planes in the azimuthal direction. Unless otherwise stated, reported results correspond to the finer mesh. Additionally, further tests were also conducted using different meshes to confirm the trends observed. These results are not shown as they do not provide new insights.

Inflow conditions were generated using the synthetic turbulence inflow conditions generation technique of Klein et al. [42, 43]. Mean velocities and turbulent intensities were made to fit those experimentally reported [40]. A pressure outlet condition is set at the outflow boundary condition and null derivatives for the other variables.

4 Results and Discussion

Results are presented in two steps in order to highlight the effects of all considered models. First, the turbulent eddy diffusivity model used is assessed. In this part, the combustion model is fixed. As pointed out earlier, a mismatch in the subgrid closures leads to an artificial lift-off of the flame. Consequently, in this part the classical flamelet model is used in order to fix the flame at the fuel nozzle rim. Afterwards, a turbulence model is selected and the different subgrid closures for the mixture fraction variance and subgrid scalar dissipation rate are analysed. The effect of the flame lift-off on the core jet is also discussed. Throughout the analysis, considerations regarding combination of different turbulence subgrid closures and different models for Z_v and χ_{sgs} models are made in order to highlight the need for consistent subgrid modelling.

4.1 Turbulent fluxes closure

Three different eddy viscosity models, based on different invariants of the strain tensor, for the Reynolds stress tensor are selected for the present analysis: the Dynamic Eddy Viscosity (DEV) [1, 2], which is based on a strain invariant, the Wall-Adapting Local Eddy-viscosity (WALE) [28], which is based on strain and rotational invariants, and the QR [29], based on the q and r strain invariants. Regarding the usage of the subgrid scale (sgs) models, for the DEV model the least-squares minimisation with averaging over homogeneous directions proposed by Lilly [2] is applied. Regarding the constant of the WALE model, a value of 0.325 is used [44]. This value is obtained if it is assumed that the WALE model gives the same ensemble average subgrid dissipation as the Smagorinsky model, where the constant for the latter is taken to be 0.1 [45].

Concerning the closure for subgrid scalars fluxes, two options are considered, use of a constant turbulent Schmidt number or a dynamically evaluated one [5], which is based on the same invariant as the DEV model. The former ensures consistency between momentum and scalars, regardless of the subgrid model for momentum. The latter is consistent only when the viscosity is evaluated also dynamically. Use of eddy viscosity models relying on different invariants, as in the WALE and QR models, results in an inconsistency among models, leading to excessive diffusion, as shown in Fig. 2, where the radial profiles of the mixture fraction and axial velocity at an axial distance located at 5 nozzle diameters from the fuel jet nozzle ($y/D = 5$) are shown. Results were computed using the coarse mesh. Nonetheless, simulations on the finer mesh yielded the same trends. In Table 2 the different combinations considered in the present analysis are listed.

On the one hand, the dynamic model applied to all variables (sgs3) shows the best agreement with the experimental data. On the other hand, combinations of the WALE or QR

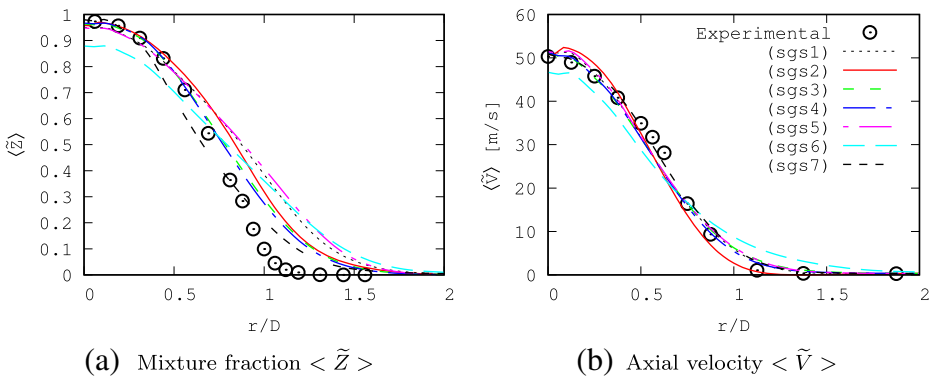


Fig. 2 Time averaged distributions at $y/D = 5$ using different combinations of subgrid closures for the unresolved turbulent fluxes. Results correspond the coarse mesh. See Table 2 for a detailed explanation of the legend

models with either a Schmidt number dynamically evaluated (*sgs1*, *sgs5*) or constant (*sgs2*, *sgs6*) showed higher deviations at the curve tail. Both QR and WALE models coupled with a dynamically evaluated mixture fraction diffusivity show a widened profile. In these cases, the turbulent subgrid fluxes for the progress-variable could not be performed with a dynamic Schmidt number, based on the strain invariant because the simulations became unstable. Consequently, in these cases a constant turbulent Schmidt number was used for $D_{c,t}$, while retaining the dynamic evaluation for $D_{Z,t}$ (*sgs1*, *sgs5*). A further simulation (*sgs7*) was conducted where the dynamic procedure for the turbulent Schmidt numbers used the WALE operator (see Appendix A for more detail of this operator). In this case, simulations are stable. Hence, using a different set of invariants between momentum and scalars and then applying a dynamic procedure to a non-conserved quantity, such as the progress-variable, may lead to modelling inconsistencies which in the end cause the simulation to diverge.

When a constant turbulent Schmidt number is used, the WALE model shows a behaviour close to the DEV applied to both momentum and scalars. Therefore, model consistency appears to be important in order to properly evaluate turbulent fluxes and limit the effect of the diffusivity introduced by the turbulence model. Still, the simulation where the WALE

Table 2 Turbulent subgrid closures combinations represented in Fig. 2

| Label | Momentum (μ_t) | Mixture fraction ($D_{Z,t}$) | Progress-variable ($D_{c,t}$) |
|-------|----------------------|--------------------------------|---------------------------------|
| sgs1 | WALE | Dyn. Sct | Sct |
| sgs2 | WALE | Sct | Sct |
| sgs3 | DEV | Dyn. Sct | Dyn. Sct |
| sgs4 | DEV | Sct | Sct |
| sgs5 | QR | Dyn. Sct | Sct |
| sgs6 | QR | Sct | Sct |
| sgs7 | WALE | *Dyn. Sct | *Dyn. Sct |

For the scalars, “Dyn. Sct” indicates a dynamically evaluated turbulent Schmidt number based on the strain invariant, as in the DEV model, whereas “Sct” indicates the use of a constant turbulent Schmidt number. The “*Dyn” indicates also a dynamic evaluated coefficient. However, it denotes that the dynamic procedure is based on the WALE operator. See Appendix A for a detail of the WALE operator

model was applied to momentum and a dynamic procedure based on the WALE invariants ($sgs7$) was used, showed mixed success. The velocity profile is in agreement with the experimental data. However, the dynamic process using the WALE invariants did not result in improved results. Further analysis would be required and comparison against DNS data would be the best approach to fully understand this behaviour.

Based on these findings, and to minimize the computational requirements, the WALE and DEV models with a constant turbulent Schmidt are mainly used. Furthermore, since the WALE model does not require an explicit filtering operation, thus minimizing the computational costs, it is the preferred approach in the following.

4.1.1 Flame stabilisation

Before proceeding to analyse the effect of the models for the subgrid mixture fraction variance and subgrid scalar dissipation rate, the effect of the flamelet database and turbulence model choice is shown in Fig. 3. Both SFPV and classical flamelet are used. Subgrid mixing is modelled through the VTE, where the turbulent viscosity to evaluate the turbulent time-scale is employed, see Table 1 for the equations involved. Additionally, a snapshot of one simulation using the LEA closure is also shown to illustrate the influence of the subgrid mixing model.

In Fig. 3 the results are obtained with the finer mesh using the WALE and DEV models together with a constant Schmidt number. As it can be seen, when the SFPV database is used together with the DEV subgrid model, an attached flame results. However, when the WALE model with SFPV is used the flame lifts-off, although experimentally it does not. Specific tests were also carried out to assess the influence of the value of the WALE model constant.

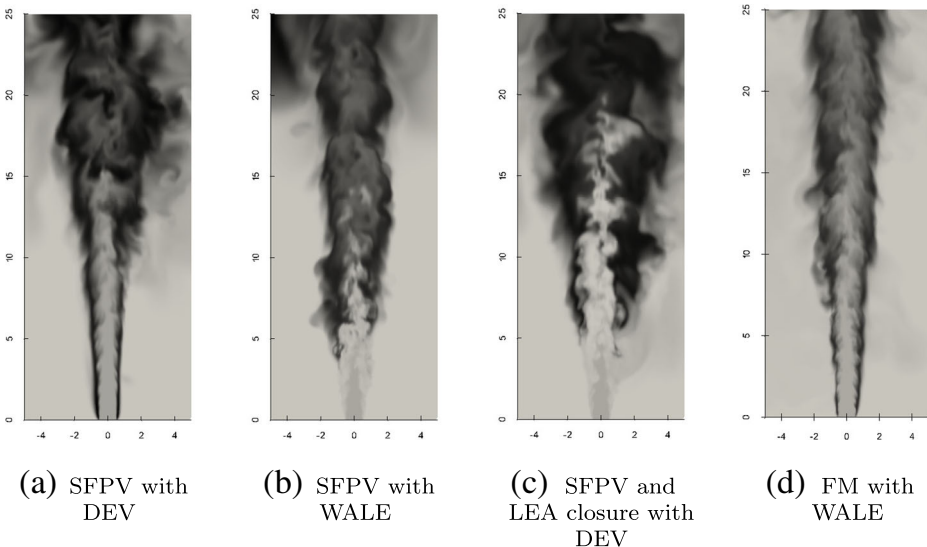


Fig. 3 Snapshots of the instantaneous progress-variable using different combinations of the FPV database and subgrid fluxes closure. The VTE closure is used except where otherwise noted. Axes lengths have been normalised using the jet inlet diameter D . Black coloration indicates a higher value of the progress-variable

No influence was found regarding the flame lift-off. Results with the classical flamelet FM are also shown in order to highlight that a reduced combustion model, in this case a database containing only ignited solutions, overshadows subgrid modelling issues.

The reason for this difference in behaviour between cases with different subgrid turbulence viscosity model can be attributed to the algebraic relation which relates Z_v with χ_{sgs} . In (16), the turbulence time-scale is related to a Smagorinsky-like subgrid dissipation and subgrid kinetic energy. When both turbulent viscosity and diffusivities are modelled using the DEV model, there is a consistency between closures. However, when the WALE model is used, different invariants are used for the turbulent viscosity and diffusivities and for the Z_v and χ_{sgs} closure. This aspect is further discussed afterwards.

Still, the other models for Z_v and χ_{sgs} presented in Section 2.2.1 also play a significant role in the correct capture of the flame stabilisation. Regardless of the turbulence model, as depicted in Fig. 3c, the algebraic relation is found not to be able to correctly describe the subgrid variance and consequently leading to a lifted-flame. For the VTE and STE models, the algebraic relation (16) is found to have a central role in the predictions, which links the model to the turbulence closure. Further discussion is presented in the following sections.

Simulations using extended flamelet databases, such as the Unsteady Flamelet/Progress-Variable model [46] were also performed to assess possible transient effect. However, it is found that the unsteady database behaves similarly to the steady model. Since the experiments reported an attached flame and low local extinction the numerical simulation should rapidly be accessing solutions close to the stable burning branch. Thus, transient ignition or extinction effects should not be significant for this case. Still, opposite to the classical flamelet model, the SFPV database is able to represent partially ignited and extinguished states.

Further simulations using different meshes were also run in order to ascertain that the observed phenomenon, flame lift-off, was not affected by the choice of filter size. Mesh variations included doubling the mesh resolution in the azimuthal-direction, using different unstructured meshes with a refinement near the fuel nozzle. Besides, the reported phenomenon was also observed on the unstructured coarse mesh when the SFPV database was used.

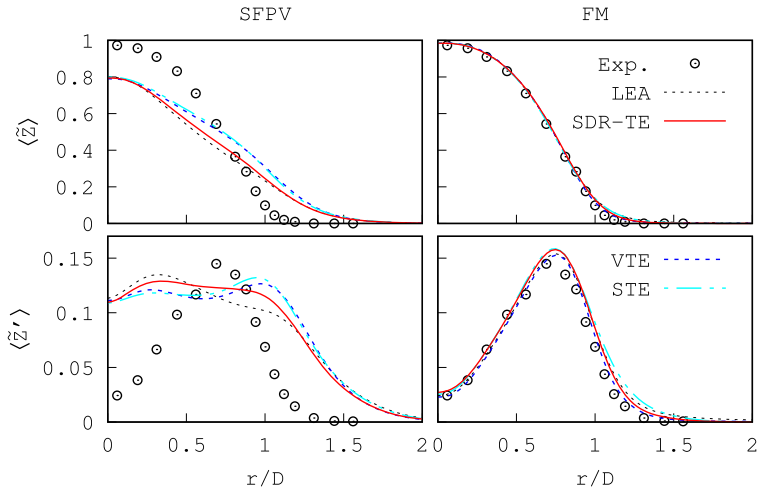
Previous studies using the DLR flame A did not report such modelling difficulties. Reported simulations using LES with flamelet modelling used a limited number of flamelet solutions, one flamelet in the study of Wang and Pope [19] and only the upper steady branch solutions by Ihme [23]. In the latter a similar behaviour to the one here described, flame lift-off, is reported, which was corrected by using the classical flamelet approach as here described. Several studies can be found in the literature in the context of RANS simulations: an Eulerian Particle Flamelet model [20], *pdf* models [17] and MMC [18]. Hence, stabilisation was either shadowed through a limited combustion subspace or through turbulence modelling.

4.2 Effect of the subgrid mixing closures

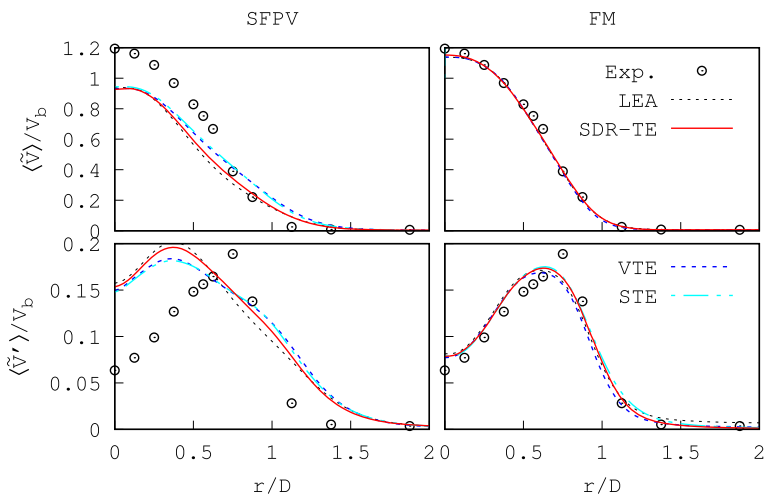
In this part of the study, the WALE subgrid model is used for all simulations. Despite the better performance of the DEV model in one case shown in Fig. 3, flame lift-off is still observed with some of the other subgrid mixing models. Then, for the sake of computational performance the WALE model is used throughout this part of the analysis. The focus in this part is to comparatively analyse the behaviour of each subgrid mixing model.

4.2.1 Lift-off effect

Before proceeding to the analysis of the different subgrid models, the effect of the flame lift-off on the fuel jet is shown. Radial profiles of the mixture fraction and axial velocity at $y/D = 5$ using the different variants of the FPV model and the four subgrid mixing closures are shown in Fig. 4. Radial profiles for two quantities are shown, the resolved mixture fraction $\langle \tilde{Z} \rangle$, its resolved root mean square (rms) $\langle \tilde{Z}' \rangle = (\langle \tilde{Z}^2 \rangle - \langle \tilde{Z} \rangle^2)^{1/2}$, and the



(a) Mixture fraction



(b) Axial velocity

Fig. 4 Radial profiles at $y/D = 5$. Results obtained using the SFPV and FM databases. Dots show data from the reported experiments [12, 13, 40]

resolved axial velocity $\langle V \rangle$ and its turbulent intensity $\langle \tilde{V}' \rangle = (\langle \tilde{V}^2 \rangle - \langle \tilde{V} \rangle^2)^{1/2}$. Temporal averaging is denoted by $\langle \cdot \rangle$. Profiles are compared against experimental data [12, 13, 40].

Due to the flame lift-off, there is a region between the fuel inlet and the flame base where the shear layer between reactant streams is not affected by the flame. It can be seen that at $y/D = 5$ both core jet mixture fraction and core velocity are noticeable lower than the experimental ones for the SFPV. Furthermore, fluctuations around the shear layer are significantly higher. However, when the flame is attached, as with the FM model, fluctuations are lower and the mean value is higher.

As reported by Clemens and Paul [47], the strong density gradients induced by flames cause a shear layer thickness reduction, which results in the jet potential core extending over longer distances. Therefore, since in the simulation the jet is not surrounded by the flame, the jet experiences higher shear and the core velocity and scalars are reduced. Profiles obtained using the classical flamelet show good agreement with the experimental data. The subgrid mixing model accounts for small differences in this regard. As it can be seen, the SFPV model, regardless of the subgrid mixing closure, predicts larger fluctuations than the experimental ones.

To further show the effect of using a reduced combustion model, scatterplots of the temperature at the fuel nozzle for two simulations are shown in Fig. 5, one using a database corresponding to the classical flamelet and the other one using the SFPV database. Results were obtained using the VTE model and the DEV model. Simulations were run on the fine mesh. Results show that on both cases only ignited flamelets are found on the lean side, as the accessed parts of the database correspond to flamelet solutions of the stable branch. However, on the rich side it can be seen that for the FM model solutions are projected towards ignited solutions, labelled in the figure as “Stable”, while for the SFPV model, transient flamelets are found for mixture fraction values away from the stoichiometric. Still, close to Z_{st} ignited flamelets are also found for the SFPV model. The difference between the SFPV and FM models is that for $Z \gtrsim 0.3$, in the latter model the retrieved temperature is higher than in the SFPV model. Therefore, density and diffusivity are lower and higher than in the SFPV model, respectively. Consequently, with the FM model, even if the flame were to lift-off, the database would still provide densities and diffusivity corresponding to ignited states. Additionally, regarding the reaction rate of the progress-variable, in the FM model only reacting states are accessed, while in the SFPV model non-reacting or extinguishing states may be accessed. Thus, the steady FM model enforces the solution to a specific set of states. It should be noted that the temperature profiles (lines) correspond to solutions where the mixture fraction variance is null. However, simulation solutions are also a function of the mixture fraction variance. Thus, the dispersion of the scatter data around the curves is due to varying levels of mixture fraction variance.

4.2.2 Subgrid mixing closures

Since the reported levels of local extinction are low for the flame at $Re=15800$ [12, 13], and in order to include most of the S-shaped solutions, but still limit the effect of the flame lift-off, a slightly modified steady FPV approach is used in the following, and is here denoted as MSFPV. This database is obtained by taking out the mixing line solution of the SFPV database. The result is that extinguishing flamelets are projected towards the lowest flamelet solution included into the database. During numerical computations, two main quantities of extinguishing/extinguished flamelets are affected, the reaction rate of the progress-variable and densities. On the one hand, the effect on the reaction rate is not significant, since at the lowest included flamelet the reaction rate is almost zero. On the other hand, the density

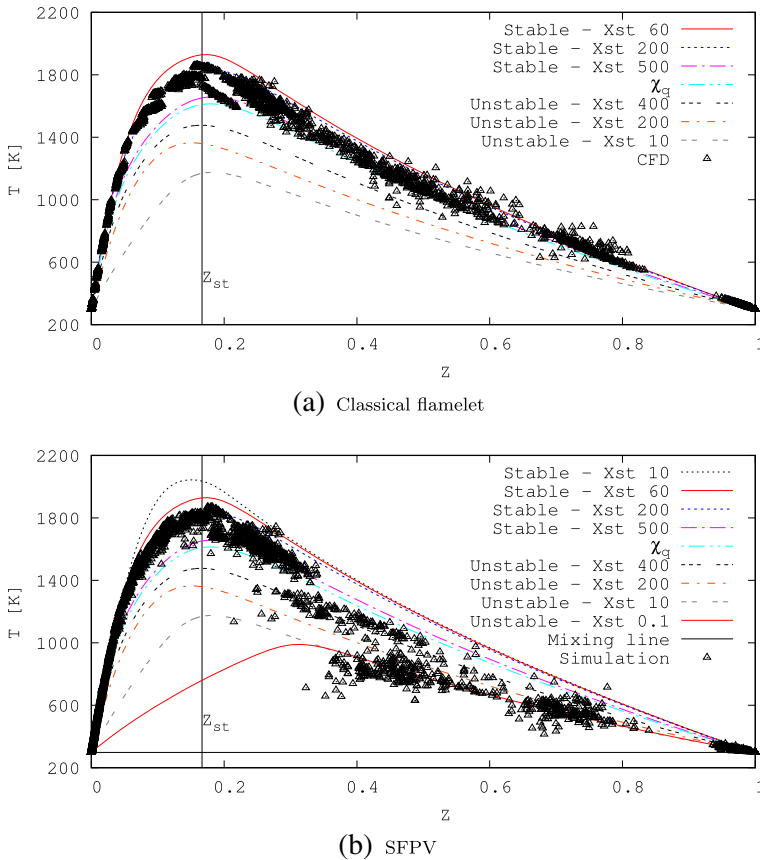
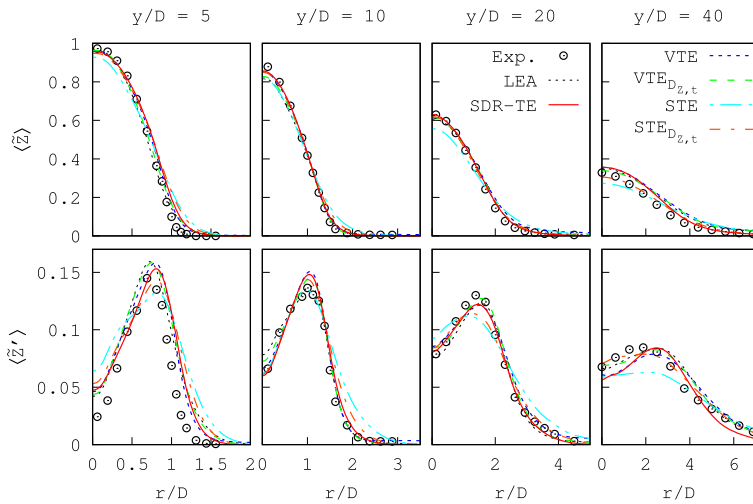


Fig. 5 Instantaneous temperature scatterplot at $y/D = 0$ for two simulations using different flamelet databases. Dots correspond to CFD simulation results. Lines correspond to flamelet solutions computed at different scalar dissipation rates, χ_{st} . χ_{q} denotes the extinction one. “Stable” denotes solutions corresponding to the upper branch of the S-shaped curve, while “Unstable” denotes the middle branch

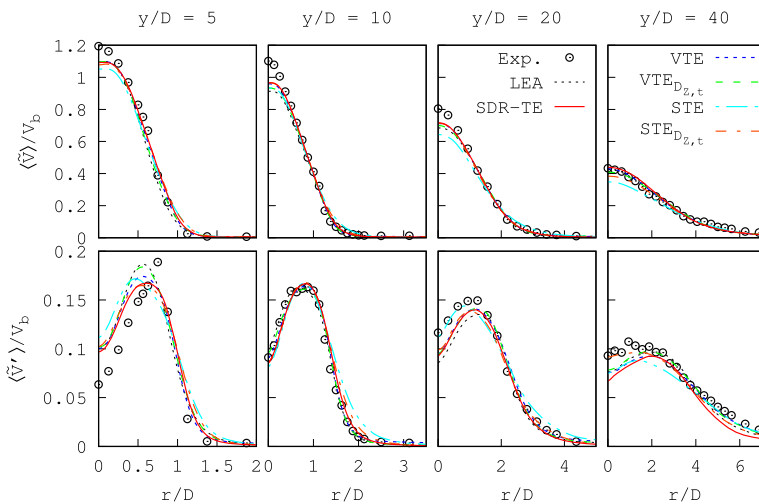
change is significant, as there is a 300-400K temperature difference between the pure mixing flamelet and the included flamelet with the smallest χ_{st} at the unstable branch. This density decrease is the aimed effect when the pure mixing solution is not included. It will result in an interface between reactant streams. Still, boundary values are not affected. This interface will mimic the effect of thermal expansion and dilatation produced by the flame as if it were stabilised at the fuel nozzle rim. Consequently, turbulent fluctuations in the shear layer are reduced, as previously shown in Fig. 4.

First are presented the time-averaged LES quantities computed using the four subgrid closures listed in Table 1. Radial profiles using the modified SFPV flamelet database at four axial locations, $y/D = 5, 10, 20$ and 40 are shown in Fig. 6. Results for the STE and VTE models are shown using ν_t and $D_{Z,t}$ as time-scales. In Fig. 7 the corresponding results using the classical flamelet of the FPV model are presented.

In general, good agreement is seen for all models. The modification in the SFPV database shows a dramatic improvement over the results in Fig. 4. Still, as it is shown in Section 4.2.3, the computed flame is not actually attached to the fuel nozzle. Nonetheless, compared to



(a) Mixture fraction

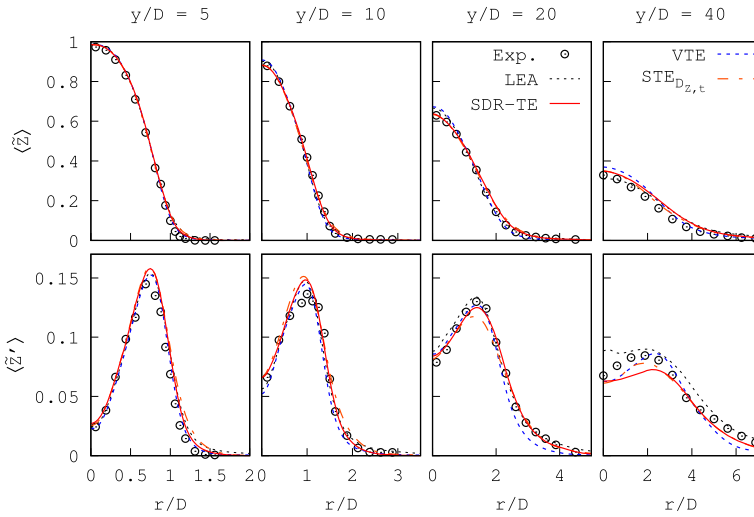


(b) Axial velocity

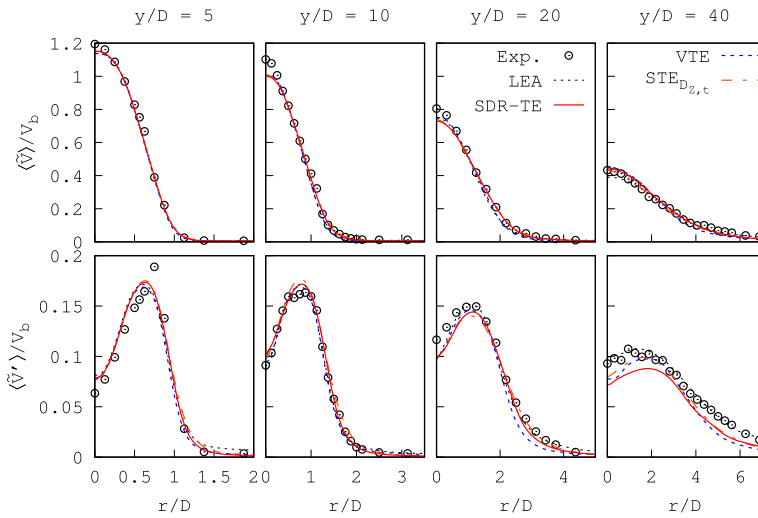
Fig. 6 Radial profiles at four axial locations. Results obtained using the MSFPV database. Dots show data from the reported experiments [12, 13]. VTE and STE models are shown using two magnitudes for the time-scale, v_t and $D_{z,t}$

the previous results, the lift-off distance is greatly reduced and the subgrid mixing closure is shown to play a significant role.

Focusing on the mixture fraction, it can be seen that the mean experimental profiles are correctly captured using both variants of the FPV model. Minor differences are observed at the tail of the curve. Regarding mixture fraction fluctuations, at $y/D = 5$ close to the axis, all mixing models result in an over-prediction of the rms with the MSFPV. Differently, the FM model results in a better description of the fluctuations. Again, the difference



(a) Mixture fraction



(b) Axial velocity

Fig. 7 Radial profiles at four axial locations. Results obtained using the FM database. Dots show data from the reported experiments [12, 13]

is attributable to the flame lift-off. The differences caused by the time-scale in the VTE and STE models are discussed afterwards. Nonetheless, the STE model is seen to deviate significantly from the experimental results.

Considering the velocities, similar trends to the mixture fraction are observed. The MSFPV model predicts higher fluctuations and a reduced core jet velocity compared to the FM model. In general, once the flame is attached, the subgrid mixing model shows a lower

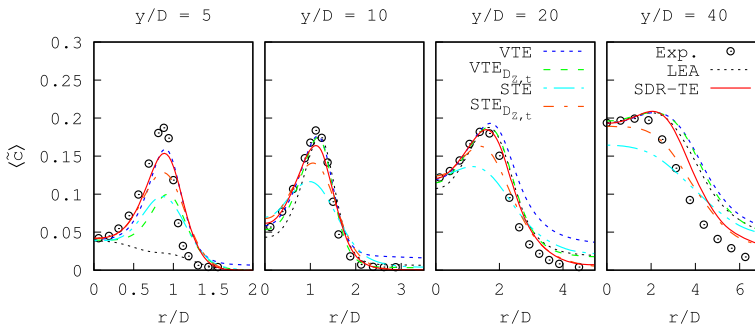


Fig. 8 Radial distributions of the progress-variable using the MSFPV database, defined as a linear summation of CO , CO_2 , H_2 and H_2O . See Fig. 6 for further explanation

effect on the converged statistics. Since the flame causes a laminarization of the shear layer, fluctuations are less pronounced.

Radial profiles of the progress-variable using the modified SFPV model, presented in Fig. 8, reveal significant differences between the different models. The influence of the sub-grid mixing model on the progress-variable is through the reaction rate, because Z_v is a parameter of the flamelet database. Hence, since the reaction rate is a function of Z_v , the progress-variable change also becomes dependent on it. Close to the jet nozzle, the mixing models play a substantial role in the correct description of the flame. Furthermore, the LEA model exhibits an almost linear distribution, indicating that the mixture is not ignited and a mixing process is taking place up to this axial location. At intermediate locations, at $y/D = 10$ and 20 , most models show good agreement with the reference data. Besides the differences due to the time-scales in VTE and STE models, minor differences can be observed close to the jet centre and at the curve tail, past the flame front. Further downstream, reaction end products ($CO/CO_2/H_2/H_2O$) are overestimated. Nonetheless, trends are in general correctly captured.

Regarding the classical flamelet, better agreement is found for the progress-variable, shown in Fig. 9, as expected from the previous discussion. Interestingly, close to the fuel

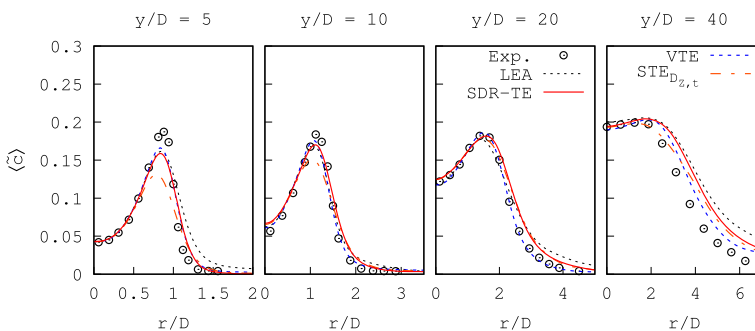


Fig. 9 Radial distributions of the progress-variable using the FM database, defined as a linear summation of CO , CO_2 , H_2 and H_2O . See Fig. 7 for further explanation

nozzle, although the shape of the profiles is correctly captured, the peak value is not. This under-prediction close to the nozzle can be explained by the set of solutions used to construct the flamelet database. Even though the flame is mostly correctly described by steady state flamelet solutions, indicating that the flame is rapidly ignited, close to the fuel nozzle there is a transition which cannot be fully represented using steady solutions. The rationale is that the reaction rates of the steady state flamelet solutions are lower than those of unsteady igniting flamelets. Consequently, since both FM and (M)SFPV databases only contain steady state solutions, the transient process is not correctly represented, which results in the peak value under-prediction. Still, at and beyond $y/D = 10$ the peak values are correctly captured, indicating that at those axial position that solutions correspond to steady state flamelet solutions, as it can be seen in Figs. 8 and 9.

Turbulent time-scale in VTE and STE models The choice of time-scale for both VTE and STE models in (16), or change in the model constant, has a significant effect, as previously shown. Nonetheless, besides the effect of the turbulent subgrid model, an important effect in the simulation outcome can be observed between choosing the turbulent viscosity or the turbulent diffusivity. Considering a constant Schmidt number, the change can be viewed as a modification of the model constant. This constant is directly related to the destruction of variance at the subgrid level in (11). The STE model does not directly take into account production and destruction of variance at the subgrid level, but in (12) χ_{sgs} and $2\tilde{D}_Z \frac{\partial \tilde{Z}}{\partial x_i} \frac{\partial \tilde{Z}}{\partial x_i}$ are two dissipation terms. Therefore, taking into account the results in Fig. 8, where the radial profiles of the progress-variable for the STE are lower than those of the VTE, it may be inferred that the STE model predicts a higher production of subgrid variance and thus the need for a higher constant in the dissipation term. In the following section it is shown that the STE predicts a higher mixture fraction variance than the VTE. In the VTE, χ_{sgs} is also a dissipation source term. However, it has a competing effect with $2D_{Z,i} \frac{\partial \tilde{Z}}{\partial x_i} \frac{\partial \tilde{Z}}{\partial x_i}$, which is a production term. Therefore, differences in the mixture fraction gradients can lead to different effects of the χ_{sgs} closure in each subgrid mixing model. For example, it can be seen in Fig. 8 that the VTE with ν_t overestimates the progress-variable at $y/D = 20$ and 40 while the STE underestimates it. When the time-scale is changed, the profiles match better the experimental data. A downward correction for the VTE is observed whereas an upward correction for the STE is seen. However, focusing on the radial profiles at $y/D = 5$, it is observed that the VTE model seems to favour a lower value of the constant, whereas the STE model profiles match better the experimental ones if a higher value is taken. Therefore, for the VTE model a dynamic evaluation of the constant could improve the results, as proposed by Kaul et al. [10], although at the expense of an increased computational cost. The STE shows a unique trend regarding the constant.

Since in the current simulations a constant turbulent Schmidt number is used, this shift may be seen as an increase of the constant used in the algebraic relation C_Z . The value of this constant (C_Z) was obtained from analysis of the turbulent spectra and LES filter widths [9]. Furthermore, in the context of RANS simulations a value of two has been commonly used [6]. However, higher values for this constant have also been reported when the STE model was used [48].

The need for an increased constant for the STE model, compared to the VTE model, can be explained by the difference at the discrete level between these models. Kemenov et al. [26] showed that when both equations are compared in their discrete form, the STE model is found to have an extra numerical source term. This source term is a result of the inability of the STE model to enforce conservation of the square of the resolved mixture fraction

(\tilde{Z}^2) at the discrete level. Consequently, the higher constant for the χ_{sgs} model, which is a dissipation term, is required to counteract this added numerical source term.

Results using the classical flamelet also showed the described trends, albeit not so clear as in the SFPV model. Therefore, here the time-scale discussion is omitted.

Another aspect to take into account in this discussion is the choice of whether to use a constant Schmidt number or a dynamically evaluated one. If the former approach is taken, the effect is only a change (an increase) in the constant value. However, if a dynamic procedure is also applied to the turbulent viscosity, then it is not equivalent to use ν_t or $D_{Z,t}$, because the diffusive term of the mixture fraction variance transport equation does use $D_{Z,t}$. Hence, if $D_{Z,t}$ is evaluated dynamically and ν_t is used for the correlation in (16), then there appears a modelling inconsistency.

4.2.3 Stabilisation distance

The incorrect capture of the progress-variable profiles near the jet nozzle is directly related to the location of the chemically reactive zones. Figure 10 shows the both azimuthal and time averaged progress-variable reaction rate, $\langle \dot{w}_c \rangle$, where as discussed it can be seen that for all the considered models the flame lifts-off and stabilises at a certain distance from the nozzle jet. Only results using the MSFPV are shown, since the FM resulted in all cases in an attached flame. Concerning the effect of the different subgrid mixing models, the LEA model predicts the largest stabilisation distance. In contrast, models accounting for subgrid production and destruction predict shorter distances. The VTE and SDR-TE models show the shortest distances. The VTE predicts a thin and elongated reaction zone, whereas the SDR-TE results in a more compact and thicker reaction zone. The shape of the reaction rate is a direct consequence of the mixture fraction, mixture fraction variance and progress-variable distributions.

From a close inspection at the reaction rate distribution for the STE model, it can be noticed a misalignment between the reaction rate and the stoichiometric mixture fraction,

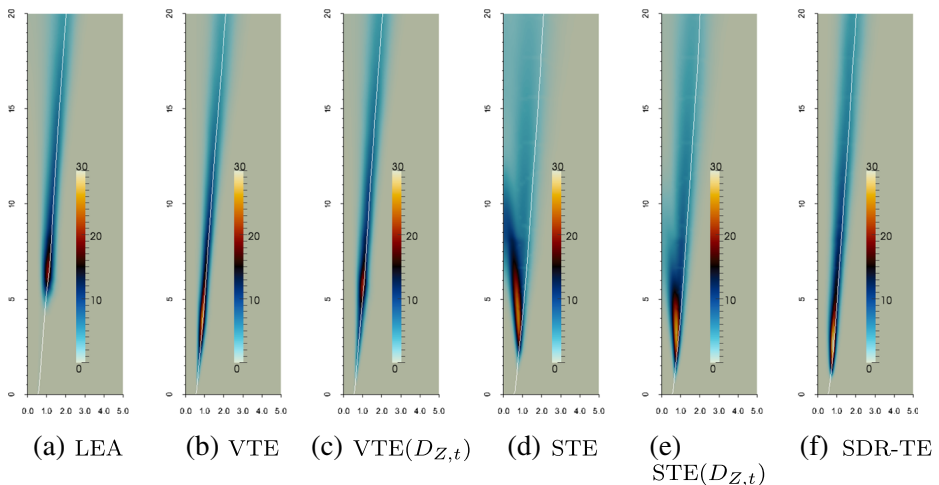
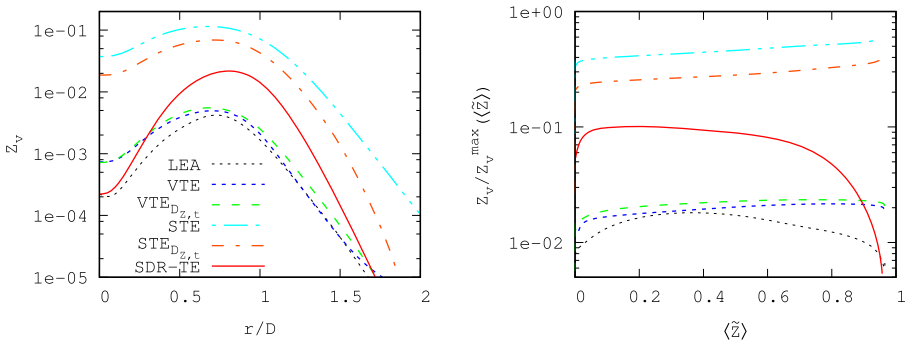


Fig. 10 Azimuthal and time-averaged progress-variable reaction rate, $\langle \dot{w}_c \rangle$ in $[kg/(m^3 s)]$. VTE and STE models computed using ν_t as time-scale. The white line marks the Z_{st} iso-contour. Results obtained using the MSFPV database. Axes lengths have been normalised using the jet inlet diameter D

leaning towards the rich side of the flame. This misalignment decreases if the turbulent time-scale is made proportional to the turbulent mixture fraction diffusivity $D_{Z,t}$, instead of the turbulent diffusivity ν_t .

This misalignment can be attributed to an over-prediction of the mixture fraction variance by the STE model. In Fig. 11 the difference in predicted mixture fraction variances between the different models at $y/D = 5$ can be observed. Results for the LEA and SDR-TE model are also displayed for completeness. The normalised mixture fraction variance is depicted in Fig. 11b, which further evidences that Z_v is significantly higher for the STE compared to the other models, for all mixture fractions. As described in the previous section, the STE model predicts a higher mixture fraction variance due to the extra numerical source term. In the following it is argued that this large values of variance across all mean mixture fractions is found to be the reason for having non-null reaction rates away from the stoichiometric mixture fraction. Additionally, snapshots of the average and instantaneous mixture fraction variance are shown in Fig. 12. Besides the stated higher variance levels predicted by the STE model compared to the VTE model, it still can be observed that at any axial section the STE model results in a Z_v field with a similar spread compared to the VTE model, that is, the mixture fraction variance is non-null for a similar range of mean mixture fractions. Oppositely, the SDR-TE shows a lower spread. The change from ν_t to $D_{Z,t}$ reduces the peak value, although it only has a minor effect on the spread. As a result, VTE using ν_t and STE using $D_{Z,t}$ mixture fraction variance predictions are qualitatively more similar, as evinced by Fig. 12b and c. Still, the actual values differ significantly. In contrast, results for the SDR-TE model show a high mixture fraction variance values are obtained close to the fuel inlet. However, Z_v reduces rapidly and reaches similar values to those of the VTE model. Still, as stated, a narrower Z_v distribution is found for the SDR-TE. Considering this wide spread together with higher Z_v values, the misalignment can be explained taking into account the reaction rate distribution for different mixture fraction variance levels, as depicted in Fig. 13. As it can be seen in the figure, for large variance levels, the reaction rate increases at high mixture fractions and decreases around the stoichiometric mixture fraction. Hence, for the STE, due to the large computed Z_v the reaction rate around the stoichiometric mixture



(a) Radial distribution of the average mixture fraction variance. (b) Normalised mixture fraction variance as a function of the averaged mixture fraction. The normalisation is performed through $Z_v^{max}(\langle \tilde{Z} \rangle) = \langle \tilde{Z} \rangle (1 - \langle \tilde{Z} \rangle)$.

Fig. 11 Mixture fraction variance at $y/D = 5$. Results obtained using the MSFPV database using the different subgrid mixing models. The vertical axis is in logarithmic scale for better visualisation

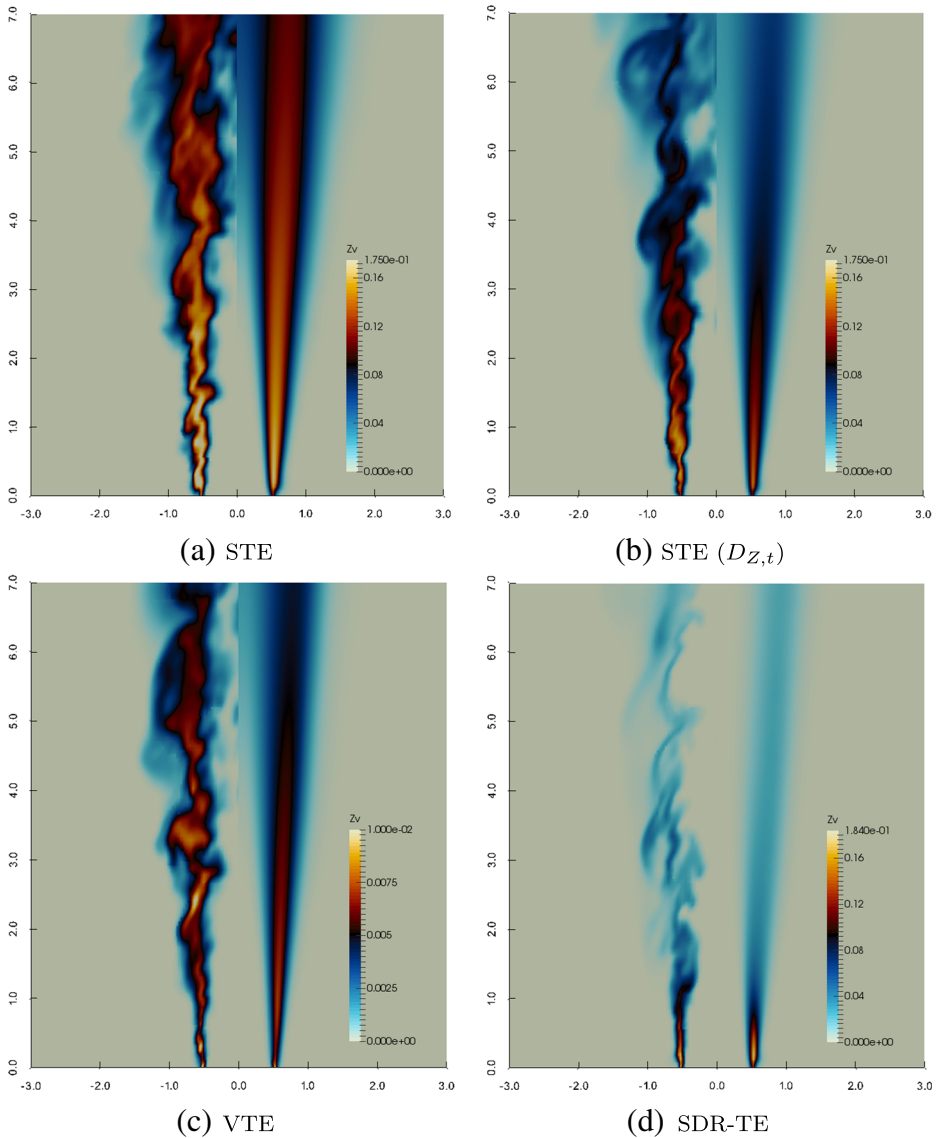
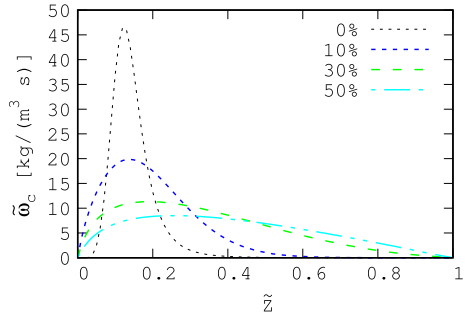


Fig. 12 Snapshot of the instantaneous (*left*) and average (*right*) mixture fraction variance Z_v close to the fuel inlet. Results obtained using the MSFPV database using the different subgrid mixing models. Axes lengths have been normalised using the jet inlet diameter D

fraction is significantly decreased, while at mixture fractions away from the stoichiometric one it is increased. Consequently, the increase in the turbulent time-scale constant leads to a reduced mixture fraction variance, see Fig. 11, which partly corrects the misalignment between the progress-variable reaction rate and the stoichiometric mixture fraction due to the decrease in the computed Z_v , see Fig. 10. Oppositely, for the VTE model, it is found that the increase in the time-scale results in the reaction zone of the flame being located at higher axial distances, see Fig. 10.

Fig. 13 Filtered reaction rate \tilde{w}_c of flamelet with $\chi_{st} = 50$ of the unstable branch for different variance levels. Each line corresponds to a percent of the mixture fraction variance and its maximum $Z_v/Z_v^{max}(\tilde{Z}) = Z_v/(\tilde{Z}(1 - \tilde{Z}))$



Despite the flame being detached from the nozzle flow, once the flame is ignited the profiles obtained match closely the experimental ones. At $y/D = 5$ in Fig. 8 the value of the computed progress-variable is lower than the experimental ones. However, at $y/D = 10$, the numerical profiles closely match the experimental ones. Furthermore, at $y/D = 40$, there is a slight overshoot in the numerical profiles with respect to the experimental ones.

4.2.4 Stabilisation distance and model consistency

It has been shown that the time-scale used for the evaluation of the subgrid scalar dissipation rate (χ_{sgs}) plays a central role in the VTE and STE models. Furthermore, it had been shown that when using these models and evaluating viscosity and diffusivities with DEV resulted in an attached flame, see Fig. 3. It had been argued that the reason was a mismatch between closures for the subgrid dissipation and subgrid kinetic energy. Consequently, the model

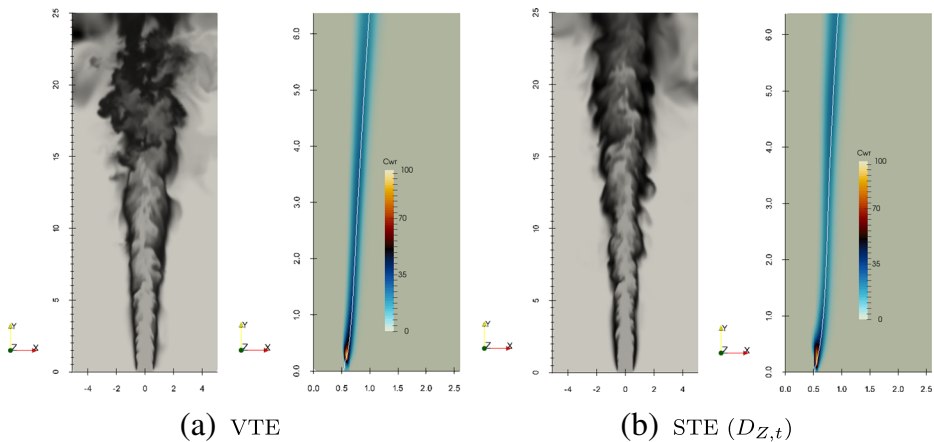


Fig. 14 Progress-variable (left) and averaged progress-variable reaction rate (right) computed using the WALE sgs model and the constant for the subgrid kinetic energy evaluated using (20). The white line marks the Z_{st} iso-contour. Results obtained using the SFPV database. Axes lengths have been normalised using the jet inlet diameter D

used for the subgrid kinetic energy has to be adapted when using a subgrid turbulence model different than the Smagorinsky or the DEV. In the present case, the aim is to modify the subgrid kinetic model so that it is consistent with a subgrid dissipation modelled using the WALE sgs model. Retaining the model for the subgrid kinetic energy

$$k = 2C_k \Delta^2 \tilde{S}_{ij} \tilde{S}_{ij} \tag{19}$$

but adjusting the model “constant” to (please see Appendix A for the derivation)

$$C_k^{3/2} = \frac{C_w^2 S_d}{C_\epsilon |\tilde{S}|} \tag{20}$$

where S_d is the WALE operator ($v_{t,w} = C_w^2 \Delta^2 S_d$) and C_ϵ is a model constant.

Simulations using both STE and VTE models using the WALE viscosity model and in (17) evaluating the turbulent subgrid kinetic energy using (20) resulted in attached flames. Note that now the full SFPV database is used. Figure 14 shows screenshots for these two cases of the averaged reaction rates and instantaneous progress-variable, respectively. In the present case, the VTE used the turbulent viscosity (v_t) and the STE used the turbulent diffusivity ($D_{Z,t}$). When the subgrid kinetic energy is consistently modelled with the subgrid dissipation, simulations result in an attached flame.

Regarding the misalignment observed previously, it can be seen that it is still present, albeit not so marked as when the flame was lifted.

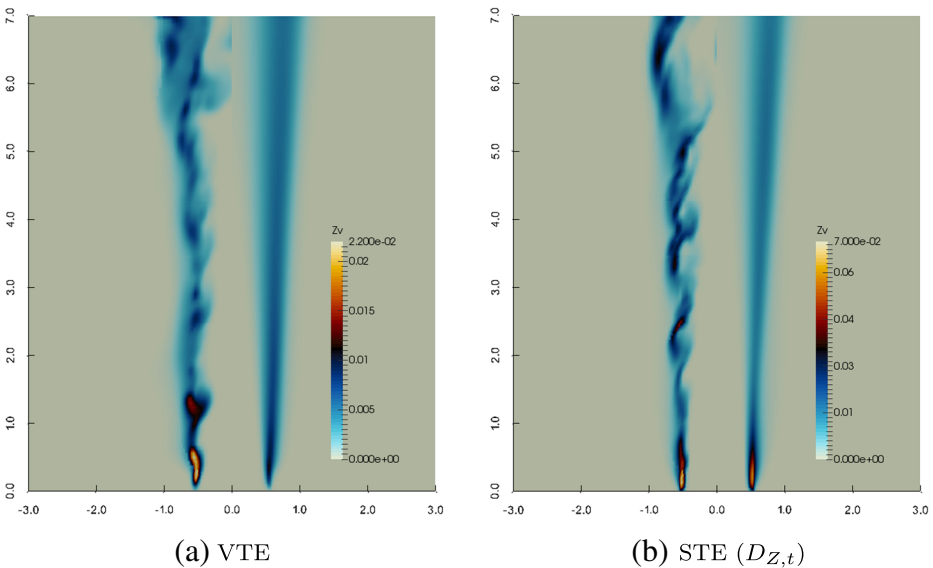


Fig. 15 Snapshot of the instantaneous (*left*) and average (*right*) mixture fraction variance Z_v close to the fuel inlet. Results obtained using the SFPV database using the different subgrid mixing models and with the change of the kinetic energy constant, (20). Axes lengths have been normalised using the jet inlet diameter D

With the previous adjustment, it is found that the predicted mixture fraction variance fields by the VTE and STE models are in much better agreement. In Fig. 15 can be seen the instantaneous and averaged Z_v fields for the same two cases as described in the previous paragraph. Consequently, it can be concluded that the mismatch between subgrid dissipation and kinetic energy closures has a higher influence on the STE than in the VTE model. In turn, this mismatch results in different computed Z_v fields by the two models. With the change of the kinetic energy constant, (20), the mixture fraction variance predicted by the STE model is greatly reduced, as can be seen by comparing Figs. 12b and 15b. Still, differences between VTE and STE can be observed, specifically in the maximum value and the field spread. Nonetheless, with the proposed modification improved agreement is found between the two models.

5 Concluding Remarks

The effects of combining different models applied to different flow phenomena have been studied in the context of a $CH_4/H_2/N_2$ turbulent diffusion flame, modelled through a Flamelet/Progress-Variable (FPV) model. Three modelling aspects have been considered: turbulent momentum subgrid fluxes, turbulent scalar subgrid fluxes and subgrid mixing in the context of a FPV combustion model.

First, it has been found that, given a combustion model, use of different subgrid closures for the Reynolds stress tensor and the scalars subgrid fluxes led to more diffused profiles. However, when closures were consistently based on the same invariants, simulation results were in better agreement with the experimental data.

Second, in the analysis of the different subgrid mixing models, where the turbulence model was fixed, revealed that numerical flame lift-off was mitigated when non-equilibrium effects were taken into account. The LEA approach resulted in a flame stabilised far from the fuel nozzle. The SDR-TE model improved significantly the results, although with significant increased computational requirements. The VTE and STE models offer a good compromise between accuracy and computational cost. Furthermore, it has been shown that the turbulent time-scale modelling is critical for these models. In this sense, consistency between the turbulence model and the time-scale model is of utmost importance. Furthermore, regarding the constant in the time-scale, it has been found that for the STE model more accurate results are obtained when a higher value of the constant is used. Oppositely, the VTE results show better performance with a smaller value.

In closing, subgrid modelling should be consistent among each of the different flow phenomena that are being modelled in order to ensure correct description of subgrid effects, so that all subgrid models become active in the same regions of the domain. In the present case failure to ensure this modelling consistency leads to a numerical lift-off of the simulated flame. The simulation in which all models were consistent resulted in an attached flame, as experimentally reported.

Acknowledgements The present work has been financially supported by the *Ministerio de Economía y Competitividad* of the Spanish government through project ENE2014-60577-R. We would also like to thank the reviewers for their helpful comments which have led to an improved article. The authors declare that they have no conflict of interest.

Appendix A

Subgrid Kinetic Energy Modelling

The VTE and STE subgrid mixing models are closed using a turbulent mixing time-scale. It has been argued that when an Smagorinsky-like turbulence model is used, closure for the subgrid dissipation and subgrid kinetic energy is consistent. However, when another model based on different invariants is used an inconsistency appears, such as in the WALE model. In the following an analysis of subgrid dissipation and subgrid kinetic energy modelling is developed for the WALE model, but an analogous process can be performed for any other subgrid viscosity model.

Modelling the relation between subgrid dissipation and subgrid kinetic energy [27] as

$$\varepsilon_{sgs} = C_\varepsilon \frac{k_{sgs}^{3/2}}{l_m} = C_\varepsilon \frac{k_{sgs}^{3/2}}{\Delta} \tag{21}$$

where l_m represents the mixing length, which is taken to be the grid size Δ . Yoshizawa and Horiuti [49] suggest a value for the constant of $C_\varepsilon = 1.8$. The subgrid dissipation is

$$\varepsilon_{sgs} = \tilde{\tau}_{ij} \tilde{S}_{ij} = 2\nu_t \tilde{S}_{ij} \tilde{S}_{ij} \tag{22}$$

with $\tilde{S}_{ij} = \frac{1}{2} \left(\frac{\partial \tilde{u}_i}{\partial x_j} + \frac{\partial \tilde{u}_j}{\partial x_i} \right)$. Combining the last two equations and introducing $|\tilde{S}| = \sqrt{2\tilde{S}_{ij} \tilde{S}_{ij}}$

$$\nu_t |\tilde{S}|^2 = C_\varepsilon \frac{k_{sgs}^{3/2}}{\Delta} \tag{23}$$

In the following, subgrid kinetic energy is modelled as

$$k = 2C_k \Delta^2 \tilde{S}_{ij} \tilde{S}_{ij} = C_k \Delta^2 |\tilde{S}|^2 \tag{24}$$

where C_k is a model constant. For Smagorinsky-like subgrid viscosity models this is a constant value. However, for models based on invariants different than the strain, it is shown that this is not a true constant. Introducing (24) into (23) results in

$$\begin{aligned} \nu_t |\tilde{S}|^2 &= \frac{C_\varepsilon}{\Delta} \left(C_k \Delta^2 |\tilde{S}|^2 \right)^{3/2} \\ \nu_t &= C_\varepsilon (C_k)^{3/2} \Delta^2 |\tilde{S}| \end{aligned} \tag{25}$$

Thus, next it is analysed the relation between the turbulent viscosity constant and the subgrid kinetic energy constant.

Smagorinsky-like subgrid viscosity

Beginning with the Smagorinsky model [4], the turbulent viscosity is

$$\nu_t = C_s^2 \Delta^2 |\tilde{S}| \tag{26}$$

Combining the latter with (25) results in

$$\begin{aligned} C_s^2 \Delta^2 |\tilde{S}| &= C_\varepsilon C_k^{3/2} \Delta^2 |\tilde{S}| \\ C_s^2 &= C_\varepsilon C_k^{3/2} \end{aligned} \tag{27}$$

Hence, when the Smagorinsky model is used, the turbulent kinetic energy model constant (24) is a true constant. Consequently, subgrid dissipation and subgrid kinetic energy are modelled consistently.

WALE subgrid viscosity

Considering the WALE model [28], the turbulent viscosity is evaluated as

$$\nu_t = C_w^2 \Delta^2 S_d \quad (28)$$

where S_d represents the operator of the WALE model

$$S_d = \frac{(\mathcal{V}_{ij} \mathcal{V}_{ij})^{3/2}}{(\tilde{S}_{ij} \tilde{S}_{ij})^{5/2} + (\mathcal{V}_{ij} \mathcal{V}_{ij})^{5/4}} \quad (29)$$

with

$$\mathcal{V}_{ij} = \frac{1}{2} \left(\left(\frac{\partial \tilde{u}_i}{\partial x_j} \right)^2 + \left(\frac{\partial \tilde{u}_j}{\partial x_i} \right)^2 \right) - \frac{1}{3} \delta_{ij} \left(\frac{\partial \tilde{u}_k}{\partial x_k} \right)^2$$

Introducing (28) into (25) yields

$$\begin{aligned} C_w^2 \Delta^2 S_d &= C_\varepsilon C_k^{3/2} \Delta^2 |\tilde{S}| \\ C_w^2 S_d &= C_\varepsilon C_k^{3/2} |\tilde{S}| \end{aligned} \quad (30)$$

showing that the model constant for the subgrid kinetic energy should take into account the strain $|\tilde{S}|$ and the operator used by the WALE model. Thus, the model constant in this case is

$$C_k^{3/2} = \frac{C_w^2 S_d}{C_\varepsilon |\tilde{S}|} \quad (31)$$

Consequently, if C_k is set to a specific value, a true constant, when the subgrid turbulent fluxes are modelled using the WALE model, there is a mismatch in (21). As a results, the modelling inconsistency previously described appears.

References

1. Germano, M., Piomelli, U., Moin, P., Cabot, W.: A dynamic subgrid-scale Eddy viscosity model. *Phys. Fluids* **3**(7), 1760–1765 (1991)
2. Lilly, D.: A proposed modification of the germano subgrid-scale closure method. *Phys. Fluids* **4**(3), 633–635 (1992)
3. Sagaut, P.: *Large Eddy Simulation for Incompressible Flows. An Introduction*. Springer-Verlag (1980)
4. Smagorinsky, J.: General circulation experiments with the primitive equations: 1. the basic experiment. *Mon. Weather Rev.* **91**, 99–164 (1963)
5. Moin, P., Squires, W., Cabot, W., Lee, S.: A dynamic subgrid-scale model for compressible turbulence and scalar transport. *Phys. Fluids* **3**(11), 2746–2757 (1991)
6. Peters, N.: *Turbulent Combustion*. Cambridge University Press (2000)
7. Pierce, C., Moin, P.: Progress-variable approach for large-eddy simulation of non-premixed turbulent combustion. *J. Fluid Mech* **504**, 73–97 (2004)
8. Pierce, C., Moin, P.: A dynamic model for subgrid-scale variance and dissipation rate of a conserved scalar. *Phys. Fluids* **10**, 3041 (1998)
9. Ihme, M., Pitsch, H.: Prediction of extinction and reignition in nonpremixed turbulent flames using a flamelet/progress variable model 2. Application in LES of Sandia flames D and E. *Combust. Flame* **155**(1-2), 90–107 (2008)

10. Kaul, C., Raman, V., Knudsen, E., Richardson, E., Chen, J.: Large Eddy simulation of a lifted ethylene flame using a dynamic nonequilibrium model for subfilter scalar variance and dissipation rate. *Proc. Combust. Inst.* **34**(1), 1289–1297 (2013)
11. Knudsen, E., Richardson, E., Doran, E., Pitsch, N., Chen, J.: Modeling scalar dissipation and scalar variance in large Eddy simulation: Algebraic and transport equation closures. *Phys. Fluids* **24**(055), 103 (2012)
12. Bergmann, V., Meier, W., Wolff, D., Stricker, W.: Application of spontaneous Raman and Rayleigh scattering and 2D LIF for the characterization of a turbulent CH₄/H₂/N₂ jet diffusion flame. *Appl. Phys. B-Lasers O.* **66**, 489–502 (1998)
13. Meier, W., Barlow, R., Chen, Y.L., Chen, J.Y.: Raman/Rayleigh/LIF measurements in a turbulent CH₄/H₂/N₂ jet diffusion flame: Experimental techniques and turbulence-chemistry interaction. *Combust. Flame* **123**, 326–343 (2000)
14. Kempf, A., Schneider, C., Sadiki, A., Janicka, J.: Large Eddy simulation of a highly turbulent methane flame: application to the dlr standard flame. In: *International Symposium on Turbulence and Shear Flow Phenomena. TSFP DIGITAL LIBRARY ONLINE*, Stockholm, Sweden (2001)
15. Pitsch, H.: Unsteady flamelet modelling of differential diffusion in turbulent jet diffusion flames. *Combust. Flame* **123**, 358–374 (2000)
16. Emami, M., Eshghinejad Fard, A.: Laminar flamelet modeling of a turbulent CH₄/H₂/N₂ jet diffusion flame using artificial neural networks. *Appl. Math. Model.* **36**(5), 2082–2093 (2012)
17. Lindstedt, R., Ozarovsky, H.: Joint scalar transported pdf modeling of nonpiloted turbulent diffusion flames. *Combust. Flame* **143**, 471–490 (2005)
18. Vogiatzaki, K., Kronenburg, A., Cleary, M., Kent, J.: Multiple mapping conditioning of turbulent jet diffusion flames. *Proc. Combust. Inst.* **32**(2), 1679–1685 (2009)
19. Wang, H., Pope, S.: Large Eddy simulation/probability density function modeling of a turbulent CH₄/H₂/N₂ jet flame. *Proc. Combust. Inst.* **33**, 1319–1330 (2011)
20. Fairweather, M., Woolley, R.: First-order conditional moment closure modeling of turbulent, non-premixed methane flames. *Combust. Flame* **138**, 3–19 (2004)
21. Lee, K.W., Choi, D.H.: Prediction of NO in turbulent diffusion flames using eulerian particle flamelet model. *Combust. Theor. Model.* **12**(5), 905–927 (2008)
22. Lee, K.W., Choi, D.H.: Analysis of NO formation in high temperature diluted air combustion in a coaxial jet flame using an unsteady flamelet model. *Int. J. Heat Mass Tran.* **52**(5-6), 1412–1420 (2009)
23. Ihme, M.: *Pollutant Formation and Noise Emission in Turbulent Non-Premixed Flames*. Ph.D. Thesis, Stanford University, Stanford (2007)
24. Ihme, M., Pitsch, H., Bodony, D.: Radiation of noise in turbulent non-premixed flames. *Proc. Combust. Inst.* **32**(1), 1545–1553 (2009)
25. Kemenov, K.A., Pope, S.: Molecular diffusion effects in LES of a piloted methane-air flame. *Combust. Flame* **158**(2), 240–254 (2011)
26. Kemenov, K.A., Wang, H., Pope, S.: Modelling effects of subgrid-scale mixture fraction variance in LES of a piloted diffusion flame. *Combust. Theor. Model.* **16**(4), 611–638 (2012)
27. Pope, S.: *Turbulent flows*. Cambridge University Press (2000)
28. Nicoud, F., Ducros, F.: Subgrid-scale stress modeling based on the square of the velocity gradient tensor. *Flow Turbul. Combust.* **62**, 183–200 (1999)
29. Verstappen, R., Meyers, J.: When does Eddy viscosity damp subfilter scales sufficiently? In: Salvetti, M.V., Geurts, B., Sagaut, P. (eds.) *Quality and Reliability of Large-Eddy Simulations II*, volume 16 of *Ercoftac Series*, vol. 16, pp. 421–430 (2010)
30. Pitsch, H., Peters, N.: A consistent flamelet formulation for non-premixed combustion considering differential diffusion effects. *Combust. Flame* **114**, 26–40 (1998)
31. Bowman, C., Frenklach, M., Smith, G., Gardiner, B., et al.: <http://www.me.berkeley.edu/gri-mech/releases.html> (2012)
32. Jiménez, C., Ducros, F., Cuenot, B., Bédat, B.: Subgrid scale variance and dissipation of a scalar field in large Eddy simulations. *Phys. Fluids* **13**(6), 1748 (2001)
33. Kaul, C., Raman, V.G.B.H.P.: Numerical errors in the computation of subfilter scalar variance in large Eddy simulations. *Phys. Fluids* **21**(55), 102 (2009)
34. Balarac, G., Pitsch, H., Raman, V.: Modeling of the subfilter scalar dissipation rate using the concept of optimal estimators. *Phys. Fluids* **20**(91), 701 (2008)
35. Balarac, G., Pitsch, H., Raman, V.: Development of a dynamic model for the subfilter scalar variance using the concept of optimal estimators. *Phys. Fluids* **20**(35), 114 (2008)
36. Verstappen, R., Veldman, A.: Symmetry-preserving discretization of turbulent flow. *J. Comput. Phys.* **187**, 343–368 (2003)

37. Darwish, M.S., Moukalled, F.H.: Normalized variable and space formulation methodology for high-resolution schemes. *Numer. Heat Tr. B-Fund.* **26**, 76–96 (1994)
38. Borrell, R., Lehmkuhl, O., Trias, F., Oyarzún, G., Oliva, A.: FFT-based Poisson Solver for large scale numerical simulations of incompressible flows. In: *Proceedings of the 23rd Parallel Computational Fluid Dynamics* (2011)
39. Lehmkuhl, O., Pérez Segarra, C., Borrell, R., Soria, M., Oliva, A.: Termofluids: A new parallel unstructured CFD code for the simulation of turbulent industrial problems on low cost PC cluster. In: *Proceedings of the Par. CFD Conference*, pp. 1–8 (2007)
40. Schneider, C., Dreizler, A., Janicka, J., Hassel, E.: Flow field measurements of stable and locally extinguishing hydrocarbon-fuelled jet flames. *Combust. Flame* **135**(1–2), 185–190 (2003)
41. <http://www.sandia.gov/TNF/DataArch/DLRflames.html> (2012)
42. Klein, M., Sadiki, A., Janicka, J.: A digital filter based generation of inflow data for spatially developing direct numerical or large eddy simulations. *J. Comput. Phys.* **186**(2), 652–665 (2003)
43. di Mare, L., Klein, M., Jones, W.P., Janicka, J.: Synthetic turbulence inflow conditions for large-eddy simulation 18(2) (2006)
44. Lehmkuhl, O., Rodríguez, I., Baez, A., Oliva, A., Pérez-segarra, C.: On the large-eddy simulations for the flow around aerodynamic profiles using unstructured grids. *Combust. Flame* **84**, 176–189 (2013)
45. Moin, P., Kim, J.: Numerical investigation of turbulent channel flow. *J. Fluid Mech* **118**, 341–377 (1982)
46. Pitsch, H., Ihme, M.: An Unsteady Flamelet/Progress Variable Method for LES of Nonpremixed Turbulent Combustion. In: *Proceedings of the 43rd AIAA Aerospace Sciences Meeting and Exhibit* (2005)
47. Clemens, N., Paul, P.: Effects of heat release on the near field flow structure of hydrogen jet diffusion flames. *Combust. Flame* **102**(3), 271–284 (1995)
48. Mueller, M., Pitsch, H.: LES model for sooting turbulent nonpremixed flames. *Combust. Flame* **159**(6), 2166–2180 (2012)
49. Yoshizawa, A., Horiuti, K.: A Statistically-Derived Subgrid-Scale Kinetic Energy Model for the Large-Eddy Simulation of Turbulent Flows. *J. Phys. Soc. Jpn.* **54**, 2834–2839 (1985)